Driving forces in thermal barrier coatings blistering

Lara Mahfouz, Basile Marchand, Vincent Guipont, Florent Coudon, Vincent Maurel

Driving forces in thermal barrier coatings blistering

Lara Mahfouz[a,b], Basile Marchand[a], Vincent Guipont[a], Florent Coudon[b], Vincent Maurel[a,1]

[a]*MINES Paris - PSL , MAT - Centre des Matériaux, CNRS UMR 7633, BP 87 91003 Evry, France*
[b]*Safran Tech, Etablissement Paris Saclay, rue des Jeunes Bois-Châteaufort, 78114 Magny-les-Hameaux, France*

Abstract

Thermal barrier coating (TBC) systems are known to be extremely sensitive to the applied thermo-mechanical loading in terms of both microstructure evolution and of subsequent damage, leading to final failure by ceramic top-coat layer spallation. The analysis of the relationship between mechanical behavior and final failure is limited by the scatter in the experimental results. Based on a typical TBC system for columnar top-coat, this study focuses on blister evolution for pure thermal cycling. The blister is processed by LAser Shock Adhesion Test (LASAT) method. It is observed experimentally that prior to significant further interfacial debonding, the height of the blister increases with the number of applied cycles. To clarify this, a finite element analysis was developed to account for multilayer system behavior and growth strain associated to a thermal-grown oxide layer evolution. Finally, this study demonstrates that rough interfaces, elasto-viscoplastic behavior of the metallic bond-coat, and oxide growth strain are needed to model the experimentally observed evolution of the blister. Thus, the driving forces acting on bond-coat rumpling, are similar to driving forces for blister height increase and final failure of the TBC.

Keywords: TBC; EB-PVD; rumpling; growth strain; LASAT; LASDAM

Highlights

- Blisters in TBC are processed according to the LAser Shock Adhesion Test (LASAT) method;
- The height of the blisters increases with thermal cycling;
- FEA of a blister is used to test different mechanisms driving the blister height increase;
- A combination of rough interface, oxide growth, associated growth strain, and bond-coat elasto-viscoplastic behavior is needed to model this;
- This sensitivity analysis demonstrates the similarity between driving forces for rumpling and damage in TBC;

1. Introduction

The assessment of coating adhesion and its evolution in experimental conditions close to those in operation is a key challenge in order to screen the performance of new coating solutions or to estimate the lifetime before spalling of existing coatings. High pressure turbine blades are subjected to very high temperature and aggressive environment so that a thermal barrier coating (TBC) is required on the single crystal Ni-base superalloys. TBC are typically a multilayer system composed of (i) a bond-coat (BC) layer reservoir of Al to form (ii) a protective oxide layer called the thermally grown oxide (TGO) and (iii) the top-coat (TC) layer providing through its low thermal conductivity the thermal insulation. The TC is mostly made of partially stabilized zirconia or a gadolinum based layer to prevent CMAS infiltration [1]. However, measurements of the adhesion of the TC in TBC systems are particularly difficult to

*Corresponding author. Tel.: +33-1-60 76 30 03; Fax: +33-1-60 76 31 50
E-mail address: vincent.maurel@minesparis.psl.eu

address because of the extreme sensitivity of this adhesion to many parameters met in industrial applications. Among these parameters some are *intrinsic* [2]: the aging of metallic material by phase transformations (BC and substrate) [3, 4], the evolution of the TGO (thickness, roughness, ...) and the nucleation of cracks at the TC/TGO interface [5, 1]. The other parameters being *extrinsic*: the chemical composition of gases (lab air, combustion gases...), the external thermo-mechanical loading on the component, the sintering of the TC layer [6, 7] and the extrinsic impact of CMAS infiltration [8, 9]. Among the evolution of microstructure of (Ni,Pt)Al metallic bond-coat, the so-called rumpling effect is assumed to govern to a large extent damage mechanisms in TBCs [2]. This rumpling phenomenon consists in a large increase of the surface roughness of (Ni,Pt)Al, when used without top-coat, under cyclic air oxidation, due to the growth strain associated to TGO growth [10]. The phenomenon is inhibited when considering low partial pressure of oxygen, or accelerated when mechanical loading is applied in addition to thermal cycling for typical thermo-mechanical fatigue testing [11, 4, 12]. On the other hand, many authors assume that rumpling promotes interfacial decohesion of the top-coat to TGO interface, by associating local debonding and grooving to rumpling, whereas the rumpling is also inhibited by the presence of the ceramic layer top-coat [13, 14, 15]. This point is still to some extent at the assumption level, where only growth strain without top-coat layer has been demonstrated to impact the surface roughness [16].

Recently, the interest in the LAser Shock Adhesion Test (LASAT) method applied to ceramic coatings increased due to a clear easiness in use, a high sensitivity to effective adhesion threshold and a limited scatter as compared to standard methods [17, 18, 19]. Using this laser-assisted technique, a delaminated area of controlled size can be introduced as an artificial interface defect at the same location as the damage created naturally by thermal cycling, namely the TGO/TC interface [19]. It has already been shown that the damage rate in presence of this pre-defect is similar to the one observed without it [20]. Otherwise, such LASAT-induced blister evolves within room temperature mechanical testing [21], thermal cycling [20], and in the presence of a thermal gradient using burner rig facility [22]. One of the more spectacular results of pre-defect introduced by LASAT in the as-received (AR) state is as follows: submitting the blister to thermal cycling, the blister height is observed to increase drastically (from 10 to 150 µm), without significant growth of the debonded area until a certain number of cycles [19]. Above this critical number of cycles, both height and debonded diameter of the blister increased with thermal cycling up to spallation occurrence. Thus, because air thermal cycling is known to promote rumpling, this blistering is assumed to be linked to rumpling as a driving force: the first assumption is that rumpling promotes damage at the crack tip, decreasing the local stiffness by increase of the process zone size [23]. Another assumption could be made considering that the rumpling mechanism promotes blistering by modifying the stress state and finally residual stresses acting on the blister after cooling. These residual stresses play a key role in the torque applied on the blister, and then can modify its morphology, particularly its height [24]. On the other hand, the parallel could be achieved with the case of a pure mechanical loading on a blister: again, the blister height increases before interfacial crack growth [21, 23]. This point is of major interest for TBC systems, it should be understood as the elaboration of increasing available energy with cycling to meet the interfacial toughness, this latter being known to decrease with cycling [25, 26, 20].

The aim of this paper is to analyze the rumpling impact on blister driven delamination through experimental results and finite element analysis (FEA). The experimental analysis is managed according to the monitoring of blister evolution measured for different thermal cycling conditions. The FE model is based on a blister involving similar dimensions of the experimental one. Thus, different assumptions in the model are tested and compared to the actual blistering phenomenology under thermal cycling. From this dual experimental-numerical approach, driving forces involved in blister height increase are investigated.

2. Experimental methods

The chosen TBC system meets the standards for high pressure turbine blades, and is provided by Safran group: the substrate is made of Ni base single crystal superalloy of first generation, AM1 (see Table 1 for composition), the bond-coat is obtained by the APVS method by first electro-deposition of Pt and Al deposit by PVD to form a diffusion (Ni,Pt)Al coating. The TC layer is made of partially yttria stabilized zirconia processed by EB-PVD; see previous works for coating details [19].

Table 1: Chemical composition of substrate superalloy, AM1 in % except for Hf and S in ppm (from [27])

	Ni	Ta	Cr	Co	W	Al	Mo	Ti	Hf (ppm)	S (ppm)
wt%	Bal.	7.97	7.54	6.61	5.49	5.2	2.01	1.2	460-490	0.104-0.123
at%	Bal.	2.65	8.74	6.76	1.80	11.61	1.26	1.51	155-165	0.195-0.231

The samples are designed as disks of 23 mm in diameter and 3 mm in thickness, the edge of each sample being rounded to limit edge effect.

LASAT was processed using a Saga Thales system, with a typical 5.2 ns pulse. Using SEM cross-section highlights debonded area corresponding to obvious blistering of the top-coat layer, e.g. for LASAT applied in the as-received condition and further submitted to 2000 S-FCT (details will be addressed in the sequel) Figure 1(a). To analyse in a non destructive manner the initial size of the debonded area, the substrate is put on a heating plate set to 60 °C and the top-surface imaging is obtained by infra-red thermography (IRT), Figure 1(b). A clear measurement of the debonded area corresponding to local minimum surface temperature is due to the air gap between the ceramic layer and the TGO, see Figure 1(a). The interested reader can refer to previous work for further experimental details [19, 22]. Then, an optical profilometer is used to measure blister shape and height.

To define blister morphology, a perfect blister could be assessed by its height, δ, and the diameter of the debonded area, D, assuming a circular debonded area, Figure 1(a) and (b).

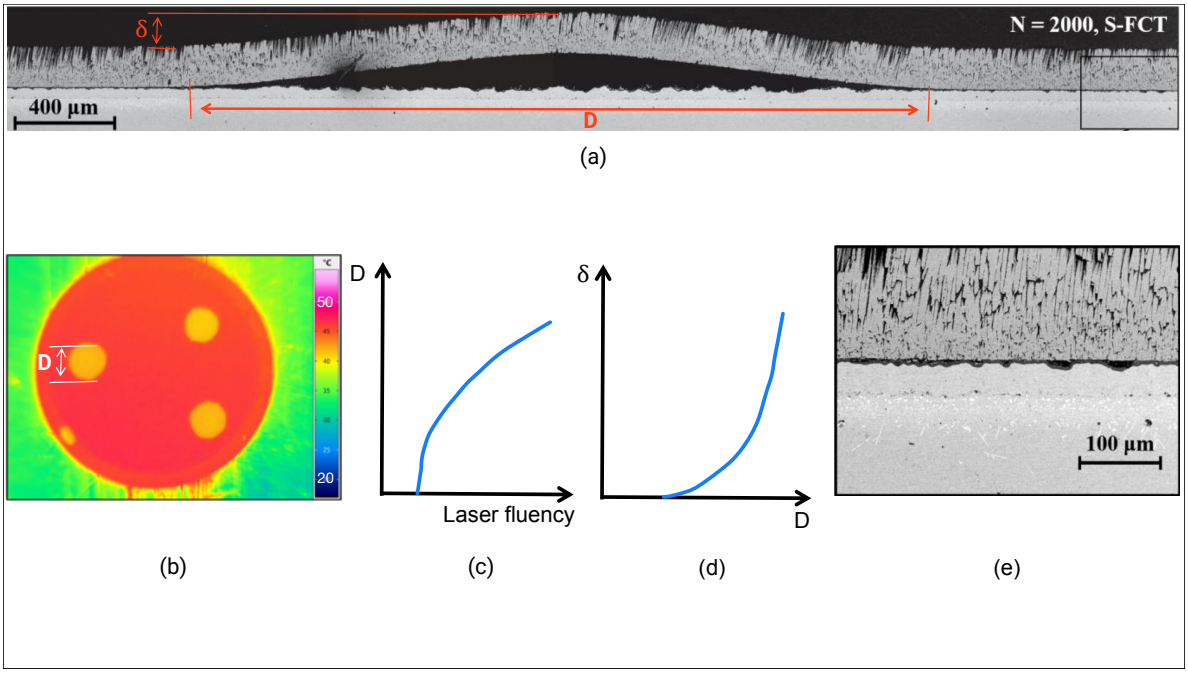

Figure 1: TBC system for LASAT specimen exposed to thermal cycling from 100 to 1100 °C using S-FCT (a) SEM cross-section (b) temperature field on ceramic side after 3 shocks processed by LASAT (c) sketch of the debonded diameter evolution with respect to the laser fluency for LASAT, (d) sketch of the blister height evolution with respect to the debonded diameter and (e) SEM detail of the microstructure far away from the location of the LASAT debonding.

For a given coating/substrate system, or in our case for a given TBC system (setting processing route and prior aging and/or thermo-mechanical loading), the debonded diameter, D, is known to be a function of the applied laser fluency during LASAT, for power beyond a given threshold, Figure 1(c). The blister height is function of the debonded diameter when freezing all other parameters (material and previous loading). It is a result of the residual stress in the system associated to the behavior of each layer involved in this process, Figure 1(d).

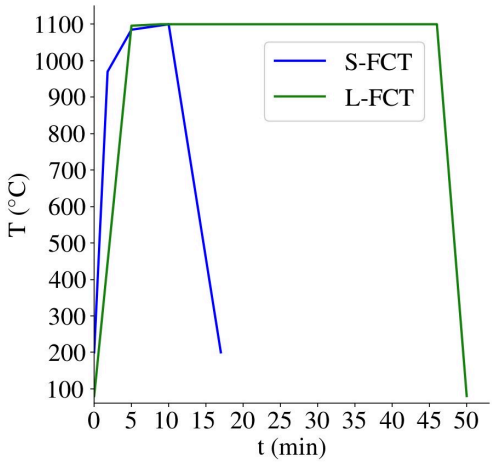

Figure 2: Thermal cycles tested in this study: long- and short furnace cycling test (L-FCT and S-FCT respectively)

LASAT was achieved either in the as-received (AR) state or after 100 thermal cycles (from 100 to 1100 °C with 50 minutes dwell at maximum temperature; long furnace thermal cycling, L-FCT), see Figure 2. Heating and cooling being achieved in approximately 5 and 4 minutes respectively.

The applied L-FCT before LASAT promotes an initial debonding localised at the TGO/TC interface after LASAT, see details in [19, 20]. By this way, further damage initiated from debonded area by LASAT will be consistent with damage localisation at the TC/TGO interface, Figure 1(e), as observed for thermal cycling of similar systems [15, 28]. Further thermal cycling was applied by short furnace thermal cycling (S-FCT), set to 100 to 1100 °C and a dwell time at maximum temperature of less than 5 minutes (rate of 3.33 °C.s^{-1}), Figure 2. To control temperature in a robust manner for S-FCT, two slopes have been applied with 430 and 35 °C/min during heating. Hence, no over heating of the sample was observed. S-FCT cycle is chosen here because it is more damaging than L-FCT for the same equivalent time spent at maximum temperature, and is closer to in service condition associated to take-off, e.g. see [20].

To summarize the different conditions tested in this study, the names of the tested specimens are as follows:

- AR: LASAT was processed in the as-received state,
- 100 L-FCT: 100 L-FCT were applied, then LASAT was processed,
- 100 L-FCT + N S-FCT: 100 L-FCT were applied, then LASAT was processed, then N S-FCT were applied, with N=871 or 2015 cycles.

3. Experimental results

First, the cross-section of a specimen subjected to 2000 short furnace cycles (S-FCT) shows that rumpling takes place in the pre-defect area (where LASAT has induced a decohesion). There, a large roughness amplitude of more than 10 µm can be observed, Figure 1(a). In areas where the TC is remaining adherent to the TGO, roughness is clearly less pronounced, Figure 1(e).

Here, for sake of clarity we only present a global analysis of the blistering effect, by plotting the evolution of the height of the blister, δ, as a function of the debonded diameter, D. In the as-received (AR) state, independently of the applied Laser shock condition, one can observe a direct correlation between debonded diameter and blister height, see red triangular marker points in Figure 3(a). After 100 L-FCT, the blisters processed by LASAT exhibit a similar correlation between debonded diameter and blister height, see yellow square marker points in Figure 3(a). Only a slight offset by lowering the height to diameter relationship is observed as compared to LASAT processed in the AR state. The differences are related to the modification of localisation of the interfacial crack: in the AR state the crack processed by LASAT is cohesive and located in the TC layer near the interface (dense part of columnar microstructure), whereas after thermal cycling the crack is adhesive and right at the TC/TGO interface [19]. For the

smallest debonded diameter, one measurement corresponds to no buckling whereas one point has a slight but clear buckling measurement of about 5 µm. This might be related to the metastable state of some delaminated areas that do not buckle.

For further cycling and considering short dwell time at maximum temperature, low number of cycles (here 871 S-FCT) are of limited impact on the height to diameter relationship, see diamonds marker points associated to S-FCT, to be compared to yellow square marker points in Figure 3(a). However, a slight increase in height is observed as compared to the trends observed at LASAT introduction. For higher number of thermal cycles (here 2015 S-FCT), the blistering has clearly increased as compared to the blister introduction by LASAT, see green square marker points in Figure 3(b).

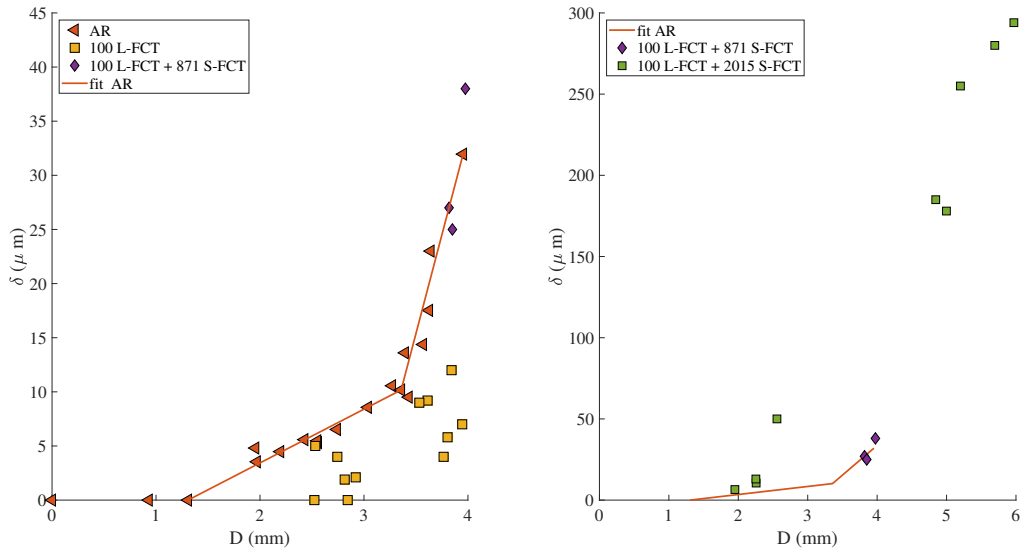

Figure 3: Evolution of blister height as a function of debonded diameter for different states (a) influence of low number of short cycles (N<900); LASAT processed in AR corresponds to [19], other data are from the current study (b) influence of low and high number of cycles (note that only fit has been reported for blisters processed in the AR)

As a concluding remark: for a given debonded diameter, results show the growth of the blister height with respect to the aging by thermal cycling. It is worthy that this result is far beyond the uncertainty level induced by both experimental facilities used for blister measurements (for diameter and height of the blister), and scatter from shock to shock, that could be related to local modification of the properties (due to either processing or damage). This evolution should be related to a strong evolution of the mechanical state in the TBC system. However, state-of-the-art mechanical analyses of blister do not propose a clear overview of the driving forces leading to this blistering effect.

On this basis, a sensitivity analysis is carried out through a full-field finite element (FE) model of the TBC system. Explicit model of the different layers and of the blister geometry in the TC layer is achieved. The idea of the next sections will be to understand what could be the mechanical driving forces at the local scale that generate an increase of the blister height (for a given debonded diameter).

4. Numerical methodology

The TBC model is composed of different layers as follows:

- the TC, assuming thermoelastic isotropic behavior;
- the TGO, assuming thermoelastic isotropic behavior and oxide growth strain;
- the BC, assuming isotropic behavior for thermo-elastic or elasto-viscoplastic model;

- the substrate, assuming thermoelastic isotropy.

The model is made of these four layers, assuming a perfect circular blister so as to consider axisymmetric condition, for a debonded radius of 1.5 mm, an initial blister height at high temperature of 25 µm and a total radius of the model of 4 mm. At the interface, the impact of an initial roughness was also studied. Based on cross-section analyses obtained by SEM, a representative initial roughness is introduced by using a sinusoidal shape of the interface with a period of 50 µm and an amplitude of 10 µm. This ondulation being homogeneous all along the interface, Figure 4(a). For comparison purpose, the same model was meshed ignoring the interfacial roughness but describing the same blister size (in terms of debonded diameter and height in the initial state). In addition to symmetry axis, set to the left end of the model, uniform radial displacement is prescribed at the right end of the model. Last boundary condition applied relates to the blistered TC and subjacent TGO surface : to avoid nodes interpenetration during thermal cycling, a mortar based penalty algorithm has been used to model contact condition between debonded TC and TGO surface [29]. The mortar method is straightforward here because the TGO surface and the inner surface of the TC layer are not conformal meshes. For the sake of simplicity, no friction is modelled within the contact.

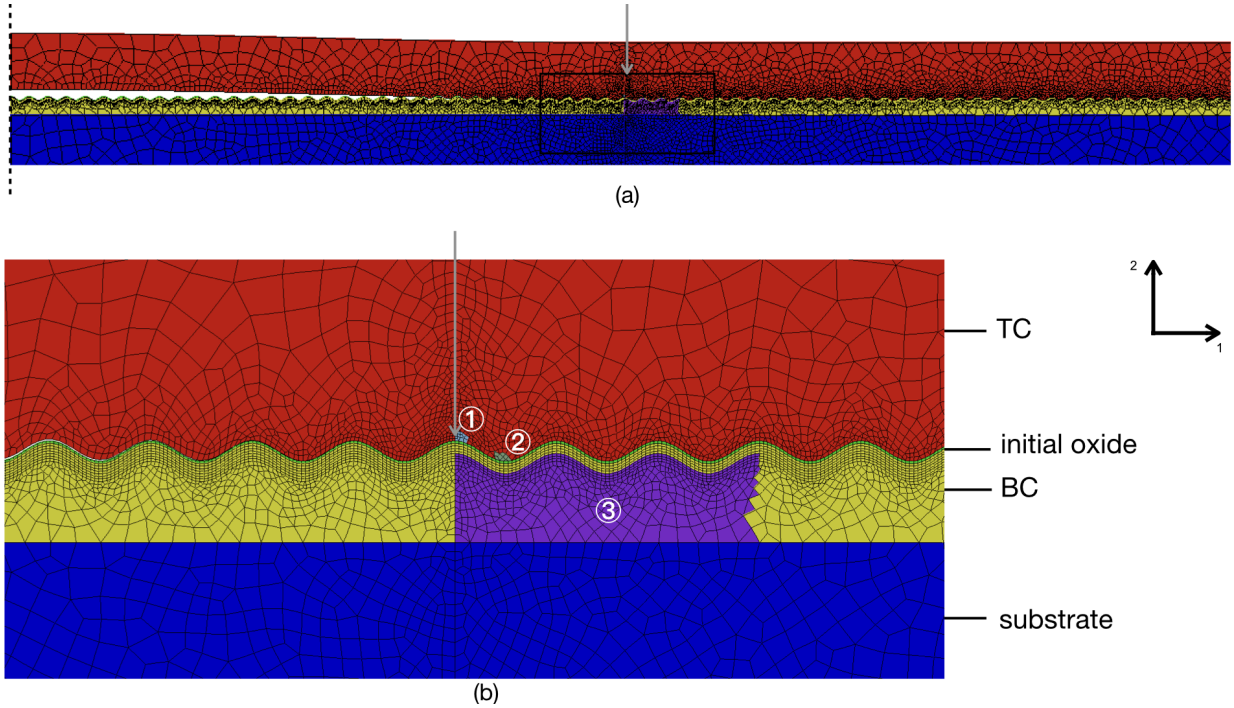

Figure 4: FE model (a) global view of the rough multilayer system (the substrate is only partially shown in thickness) (b) detail of the initial TGO layer and the BC prone to be transformed into TGO; the grey arrow corresponds to the location of the crack tip between TC and TGO layer; ①, ② and ③ correspond respectively to sets of FE elements used to average stress at top and valley in the TC layer, and strain in the BC layer (associated colors are only to point out the precise areas used for averaging).

All FEA conditions are recalled in table 2.

Oxidation kinetic is described through a parabolic growth written in an incremental form, so as to account to temperature evolution along thermal cycling [28]:

$$\frac{dh}{dt} = \frac{1}{2h}\alpha_0 \exp(-Q/RT) \tag{1}$$

where h corresponds to the oxide thickness, α_0 is a material parameter used to assess oxide growth kinetic associated to a classical Arrhenius sensitivity to temperature T, Q is the thermal activation and R the gas constant.

Growth strain is related to the transformation of BC into TGO, accounting for Pilling-Bedworth ratio. The growth strain, is represented by an anisotropic eigenstrain tensor, $\underset{\sim}{\varepsilon}_{gr}$, with the maximum of growth strain normal to the oxide

Table 2: Different model assumptions used for FEA ; $\underset{\sim}{\varepsilon}_{gr}$ corresponds to the growth strain associated to TGO growth, oxidation kinetic accelerated (acc.) or realistic (real)

Case	Interface	BC	$\underset{\sim}{\varepsilon}_{gr}$	oxidation kinetic
1	Flat	elasto-viscoplastic	yes	acc.
2	Rough	elastic	yes	acc.
3		elasto-viscoplastic	no	acc.
4		elasto-viscoplastic	yes	acc.
5		elasto-viscoplastic	yes	real

interface (here 22 in a local frame) [30, 31, 32]:

$$[\underset{\sim}{\varepsilon}_{gr}] = \begin{bmatrix} 0.003 & 0 & 0 \\ 0 & 0.27 & 0 \\ 0 & 0 & 0.003 \end{bmatrix} \tag{2}$$

This growth strain corresponds to a volume change from oxidized volume of metal V_m to oxidized volume of oxide V_{ox}, $V_{ox}/V_m \simeq 1+\varepsilon^1_{gr}+\varepsilon^2_{gr}+\varepsilon^3_{gr}$, where ε^i_{gr} corresponds to each of the diagonal components of the growth strain tensor [30]. This results in a volume change of $V_{ox}/V_m \simeq 1.28$. For sake of simplicity, only internal oxidation is accounted for.

As previously developed in [30], the oxidation consists of a progressive transformation of elements associated initially to BC to oxide, so as to account for both the transition in mechanical behavior and the contribution of growth strain. This progressive oxidation is a key point in the proposed analysis enabling to consider a continuous mechanical history [33, 34, 35], whereas most of the studies in TBC prefer to analyze separately different oxide thicknesses (e.g. [36]). Thus, the mesh is refined in an area where the BC is prone to be transformed into TGO, see Figure 4(b). The rate of transformation is associated to the oxide growth kinetics, eq. 1 by using a progressive growth of the oxide fraction within the line of elements associated to the oxide/BC interface, following the prescribed sinusoidal shape of the interface. In these elements, the global stress is defined using the local stresses evaluated for both oxide and BC behaviors, following:

$$\underset{\sim}{\sigma} = f_v \underset{\sim}{\sigma}_{ox} + (1-f_v)\underset{\sim}{\sigma}_{BC} \tag{3}$$

where f_v corresponds to the volume fraction of the oxide within the considered element, $\underset{\sim}{\sigma}_{ox}$ and $\underset{\sim}{\sigma}_{BC}$ are the stress tensors related to the oxide and the BC behaviors respectively. The local stresses, within this line of elements in transformation, are estimated using the Voigt assumption of an uniform total strain.

For the mechanical behavior of the oxide layer, the total strain tensor $\underset{\sim}{\varepsilon}_t$ is decomposed into:

$$\underset{\sim}{\varepsilon}_t = \underset{\sim}{\varepsilon}_m + \underset{\sim}{\varepsilon}_{th} + \underset{\sim}{\varepsilon}_{gr} \tag{4}$$

where $\underset{\sim}{\varepsilon}_m$ and $\underset{\sim}{\varepsilon}_{th}$ correspond to mechanical and thermal strain tensors respectively. The oxide layer is assumed to be elastic $\underset{\sim}{\varepsilon}_m = \underset{\sim}{\varepsilon}_e$.

To summarize the model assumptions for elasto-viscoplastic behavior of the BC, the constitutive equations are recalled in Table 3. The chosen model associates non-linear isotropic hardening, so as to account for slight softening observed experimentally for large strain values [37], and kinematic hardening to account for ratcheting effect associated to rumpling [38].

The low temperature thermo-elastic properties of each layer are detailed in Table 4, accounting for coefficient of thermal expansion (CTE) for each layer. Besides, details of visco-plastic parameters of the bond-coat layer function of significative temperatures are given in Table 5. The drastic modification of the yield stress, σ_Y, corresponds to observed transition into ductile behavior of typical (Ni,Pt)Al layer [40, 41, 37].

The applied loading corresponds to thermal cycling experienced by the TBC systems, but ignoring the thermal gradient within its thickness. It consists in: first cooling from the temperature applied during the top coat deposition, of 1100 °C to room temperature at a cooling rate of 3.33 °C.s^{-1}. Then heating to the maximum temperature of 1100 °C at a heating rate of 3.33 °C.s^{-1}, followed by dwell at this maximum temperature for 5 minutes and the same cooling rate down to 100 °C. The cycling from 100 °C to 1100 °C was applied 10 times.

Table 3: Set of equations used for the mechanical behavior of the BC layer. With $\underset{\sim}{\varepsilon}_m$, $\underset{\sim}{\varepsilon}_e$ and $\underset{\sim}{\varepsilon}_p$ the mechanical, elastic and plastic strain tensor respectively, $\mathcal{J}_2$ the von Mises yield function, and p is the cumulated plastic strain [39]

Strain partitioning	$\underset{\sim}{\varepsilon}_t = \underset{\sim}{\varepsilon}_{th} + \underset{\sim}{\varepsilon}_e + \underset{\sim}{\varepsilon}_p$
Yield function	$f = \mathcal{J}_2\left(\underset{\sim}{\sigma} - \underset{\sim}{X}\right) - R_0 - R$
Isotropic Hardening	$R = Q_{BC}\left(1 - \exp\left(-bp\right)\right)$
Kinematic Hardening	$\underset{\sim}{X} = \frac{2}{3} C \underset{\sim}{\alpha},\ \dot{\underset{\sim}{\alpha}} = \dot{\underset{\sim}{\varepsilon}}^p - \frac{3}{2}\frac{D}{C}\underset{\sim}{X}\dot{p}$
Flow Function	$\dot{\underset{\sim}{\varepsilon}}^p = \dot{p}\underset{\sim}{n},\ \dot{p} = \left\langle \frac{f}{K} \right\rangle^n$ and $\underset{\sim}{n} = \frac{\partial f}{\partial \underset{\sim}{\sigma}}$

Table 4: thermo-elastic parameters at 100 °C used in this study; initial thickness of each layer, h_0

	Substrate	BC	TC	TGO
E (GPa)	133.	161.	60.	395.
ν	0.34	0.33	0.1	0.22
α (10^{-6} K^{-1})	14.	15.	10.	8.5
h_0 (μm)	2000	50	125	1
Ref.	[42]	[37]	[30]	[30]

Table 5: Yield stress of the BC layer when used in this study, from [37]

Temperature (°C)	100	650	1100
σ_Y (MPa)	10 10^3	70	28

Last but not least, the chosen kinetic for oxide growth was artificially increased to limit CPU time: the oxide thickness reached 5 µm after the 10 cycles described before. The influence of this assumption will be detailed in the discussion.

5. Parameters influencing blistering

Firstly, the local out-of-plane stress is known to be directly linked to interfacial damage: this should be seen as a driving force for interfacial crack opening [36]. In our case, because the location of the crack tip is defined, several observations can be developed from the case combining interfacial roughness, elasto-viscoplastic BC and growth strain, case #4 Table 2, corresponding to the reference case. When observing the mechanical state in the debonded area after thermal cycling and at low temperature (Figure 5(a) and (b)), σ_{22} is lower than in the area where the TC is adherent to the TGO. Also, the maximum values are reached at the very crack tip. Besides, local oscillations of σ_{22} are observed along the sinusoidal profile, from compression at its peak to tension at its valley. This last point is consistent with literature observations [43, 44]. However, in the presence of the interfacial crack as experimentally tested, this sheds a new light on the observed evolution of the blister: if the crack is located at a peak of the rough interface, the compressive value of out-of-plane stress, σ_{22}, clarifies that the crack could reach a stable position. On

the other hand, if the crack is located at the valley of the local rough interface, large positive values of σ_{22} would induce a significant crack propagation.

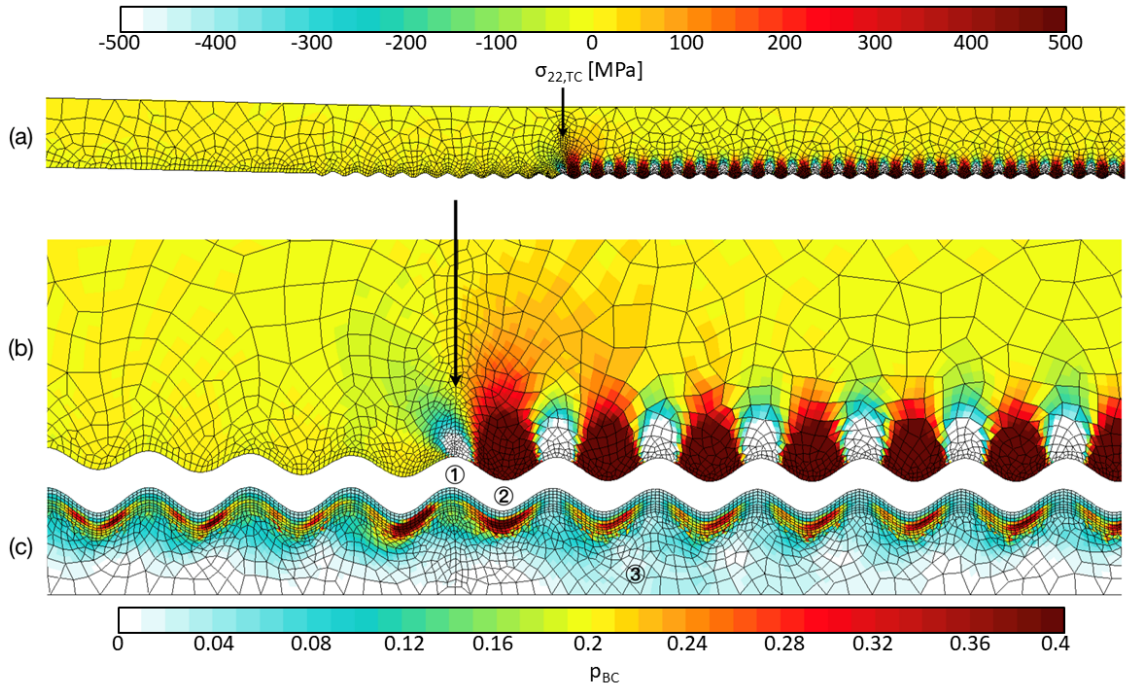

Figure 5: Out-of-plane stress component in the TC layer, σ_{22} (a) and detail in (b), cumulated plasticity in the BC layer (c) (note that the color bars correspond respectively to (a) and (b), at the top and to (c) at the bottom and that the separation between TC and TGO is artificial for visualisation purpose; the arrow indicates the abscissa of the crack tip)

However, this confirms that the crack tip should be carefully analyzed through the process zone where damage will develop [22]: this process zone corresponds to the area where the TC is adherent to the TGO, in the vicinity of the crack tip and it is the place of maximum stress. Local evolutions of mechanical quantities are thus studied within the TC layer at the crack tip for the different modelling assumptions presented in Table 2, focusing on local stress values, Figure 6a.

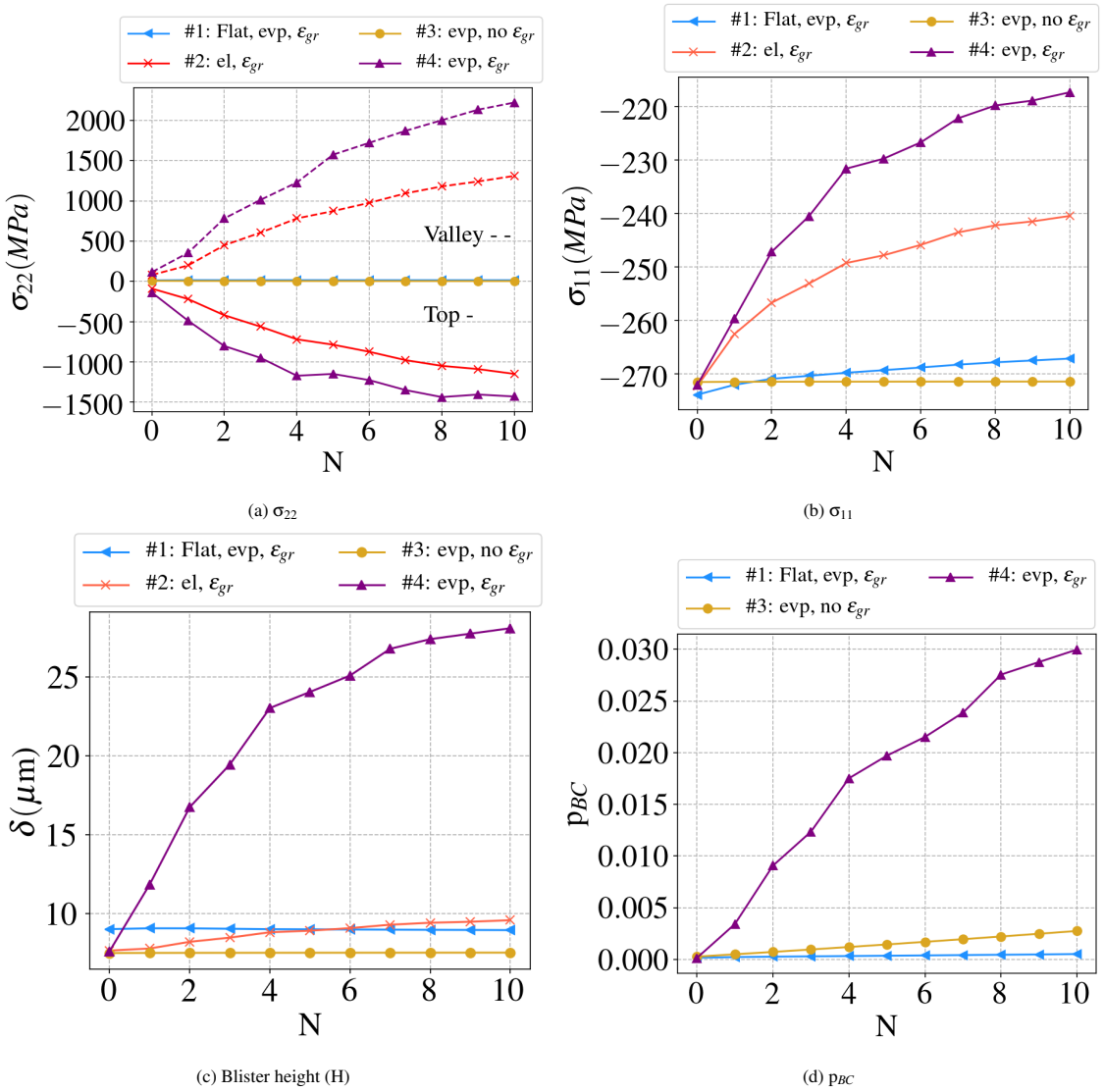

(a) σ_{22}

(b) σ_{11}

(c) Blister height (H)

(d) p_{BC}

Figure 6: (a) Evolution of σ_{22} at the crack tip and at the valley (corresponding to ① and ② respectively in Figure 4); (b) Evolution of σ_{11} averaged in the adherent part of the TC; (c) blistering and (d) cumulated plasticity in the BC (corresponding to ③ in Figure 4) for different model assumptions. Values correspond to the end of the cooling stage associated to each cycle.

The out-of-plane component, σ_{22}, reflects a driving force for local damage when positive values are reached, Figure 6a. It is worth noting that a "non-local" damage is effective in this configuration: the damage will be associated to positive values of σ_{22} at the valley, beyond the crack tip location, see dashed lines Figure 6a. Further crack propagation can only come from coalescence between the crack tip and this potentially damaged area by micro-cracking.

However, the evolution of σ_{22} at the crack tip when located at the top, reflects the coupling of roughness and growth strain, see continuous lines Figure 6a. For a flat interface with growth strain and elasto-viscoplastic BC, case # 1, no evolution is observed for the 10 cycles tested. In contrast, a drastic increase of absolute value of σ_{22} is observed for both elastic and elasto-viscoplastic BC behavior accounting for growth strain with a rough interface, cases #2 and 4. Finally, the association of rough interface, and elasto-viscoplastic BC behavior without growth strain leads to no evolution of the σ_{22} component, case #3. As a first result, the local damage seems to be driven by the combination of a rough interface and growth strain within the oxide layer, and to a lower extent by the elasto-viscoplastic behavior

of the BC layer, case #4, as compared to an elastic assumption, case #2: the absolute value of σ_{22} is observed to be higher with viscoplasticity, case #4, than with elasticity, case #2.

The in-plane component, σ_{11}, is related to the build-up of residual stresses in the TBC system during thermal cycling. This quantity is generally used to asses the impact of CTE mismatch between layers, but is also driven by growth strain and creep. Thus by averaging σ_{11} in the adherent TC layer, we can derive some conclusions, Figure 6b. Again, the evolution of σ_{11} reflects coupling of roughness and growth strain. The intensity of the in-plane compressive stress decreases significantly with cycling for a rough interface and growth strain, cases #2 and 4, with a minor effect of the BC behavior. However, a slight decrease is also observed for the flat interface accounting for growth strain, case #1, whereas σ_{11} is constant for a rough interface without TGO growth strain, case #3.

To summarize this sensitivity analysis, combining a rough interface and growth strain within the oxide layer is needed to model a significant stress evolution within the TC layer in the vicinity of the crack tip. The combination of growth strain to elasto-viscoplastic BC behavior impacts σ_{11} even when modelling a flat interface.

The experiments carried out in this context only give access to the evolution of blister height, which is observed to first increase with thermal cycling without a significant evolution of the debonded area (interfacial crack size). The proposed FEA also provides a blister evolution for a given crack length. In particular, the evolution of the blister height was plotted in the figure 6c. This leads to a major conclusion: the only way to observe an increase in the blister height, consistent with experiments, is to associate a rough interface, growth strain within the TGO and elasto-viscoplastic behavior for the BC layer, case #4. Despite the similar trends on the local stresses evolution for both elastic and elasto-viscoplastic BC behavior shown in the figure 6a and 6b, the blister height is seen to slightly increase for the test case with an elastic BC. For a flat interface, growth strain and elasto-viscoplastic BC behavior, case #1, the height of the blister decreases, exhibiting the need of a model including a local roughness. Finally, the model combining an elasto-viscoplastic BC and a rough interface while ignoring the growth strain, case #3, leads to a constant blister height.

The almost constant blister height observed during thermal cycling for an elastic BC, case #2, suggests that the increase in blister height is not simply related to the stress level at the crack tip. Thus, the plasticity level in the BC layer could clarify the impact of the chosen assumptions. In the BC layer, local maxima of σ_{22} correspond clearly to local maxima of strain localisation as can be observed from the field of the cumulated plastic strain (called p_{BC}) in Figure 5(c). Also, maxima are reached close to the crack tip, see label ② Figure 5(c). But, in addition to this, a lower but non-negligible plasticity appears in the area of the BC layer corresponding to adherent ceramic layer, close to the substrate interface and limited to few undulations from the crack tip, see label ③ Figure 5(c). This slight plasticity is vanishing away from the crack tip and could correspond for the blister to a kind of plastic hinge. By comparing the evolution of plasticity in this area for the different modelling assumptions, the evolution of blister height is clearly correlated to this strain localisation in the BC layer, Figure 6d.

6. Discussion

To summarise the above analysis, the role of boundary conditions in blister buckling shoud be discussed. The starting point is the elastic analysis of a perfect blister clamped on its edge proposed by Hutchinson et al [24].

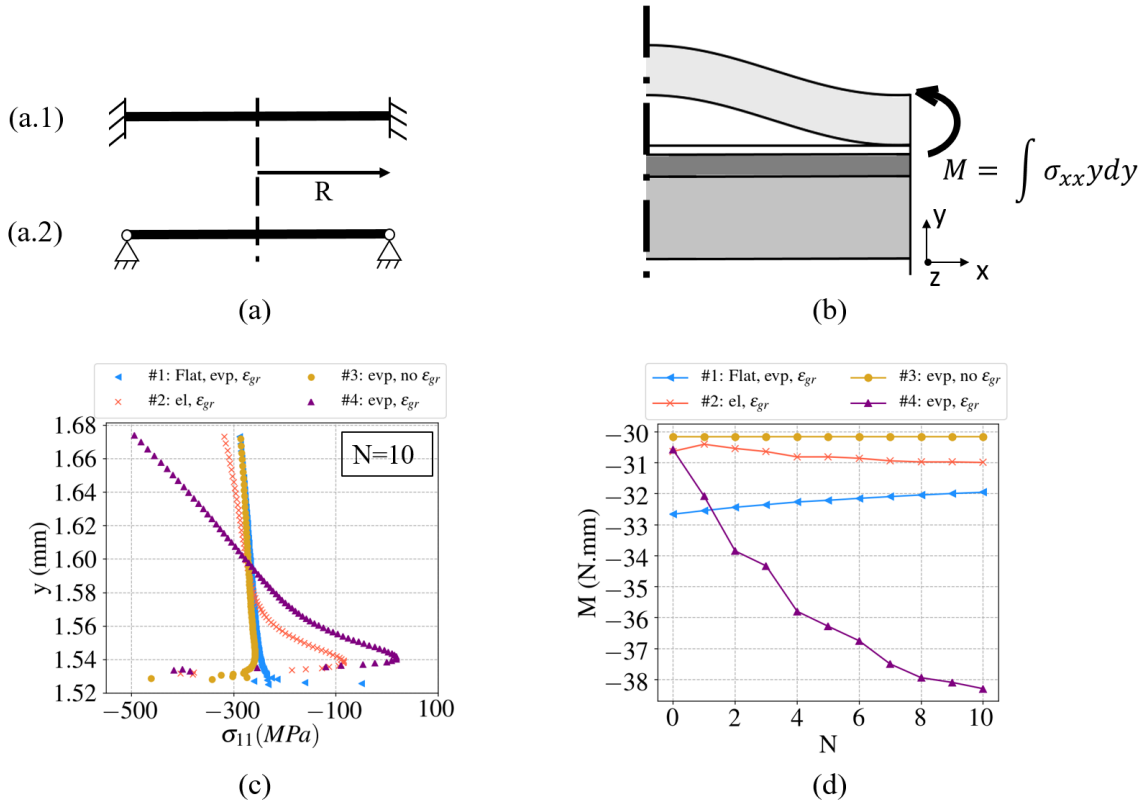

Figure 7: (a) schematic of boundary conditions (b) force and moment acting on the blister (c) evolution of σ_{11} as a function of y and (d) evolution of the torque with the number of cycles as a function of the different assumptions

The buckling is known to be strongly correlated to the boundary conditions. For a perfectly clamped structure, Figure 7(a.1), the effective radius to be accounted for in buckling analysis, R_{eff}, corresponds to the geometrical radius of the blister $R_{eff} = R$, whereas for simple contact (without torque constraint), Figure 7(a.2), $R_{eff} = 2R$. This does impact firstly the critical stress to induce buckling, σ_c, the higher the effective radius, the lower the critical stress:

$$\sigma_c = 1.2235 \frac{E}{1-\nu^2} \left(\frac{h}{R_{eff}} \right)^2 \tag{5}$$

where E and ν correspond respectively to the Young's modulus and the Poisson's ratio of the TC layer [24]. In addition, the height of the blister δ is assessed as a function of the critical stress at buckling:

$$\frac{\delta}{h} \simeq \left[\frac{1}{c_1} \left(\frac{\sigma}{\sigma_c} - 1 \right) \right]^{1/2} \tag{6}$$

where h corresponds to the height of the TC layer, σ is the in-plane stress component considering equibiaxial loading, and c_1 is a function depending of the Poisson's ratio ν, following $c_1 = 0.2473(1+\nu) + 0.2231(1-\nu^2)$. The above set of equations corresponds to a blister perfectly clamped on its edge, however in a rough approximation, from a perfect blister to simple contact boundary conditions, Figures 7(a.1) to (a.2), the critical stress is divided by 4 and thus, the height of the blister could increase by a factor of two.

The strain localization described above, and the plastic hinge, will thus induce larger buckling considering a transition from rigid boundary condition to less constraint in torque. However, the in plane stress level decreasing with the number of thermal cycles, Figure 6b, the height of the blister should decrease inconsistently with experimental observations.

It is worth noting that the in-plane stress σ_{11} along y direction, is a function of the ordinate y from the crack tip to the surface of the top-coat, Figure 7(b). This result differs to a large extent from pure bending, Figure 7(c). Besides, the sign of stress values σ_{11} is strongly influenced by the chosen modelling assumption. This point may clarify the limit of the elastic analysis derived from Hutchinson et al.

Finally, the torque, M, applied to the blister can be assessed by the integration of σ_{11} along the y direction from the crack tip to the surface of the top-coat as shown in Figure 7(b), using $M = \int_0^{h_{TC}} y \times \sigma_{11} dy$. The evolution of M with the number of thermal cycles is plot for the different assumptions in Figure 7(d). Again, only case #4 exhibits a global increase of torque with cycling: ignoring the interfacial roughness yields to a slight decrease in M, case #1, ignoring the BC plasticity yields to a slight increase but a quick saturation effect, case #2, and ignoring the growth strain yields to a constant torque, case #3. This finally proves that blister height increase is induced by modification of boundary conditions of the blister, associated to strain localization in the BC, and by a large increase in torque driving the blister height.

Last but not least, one important assumption should be analyzed: what is the influence of chosen accelerated oxidation kinetic on the evolution of mechanical state and buckling? This point is crucial in the proposed analysis by the way two kinetics should be considered: the oxidation kinetic but also the kinetic associated to viscosity and creep of the BC layer. To clarify this point, realistic oxidation kinetic has been used without modification of other parameters based on case #4 associating rough interface, visco-plasticity of the BC layer and growth strain. This constitutes the case #5. The CPU time for case #5 and 1000 cycles corresponds to 16 days, to be compared to 4 hours for case #5.

As a first salient result, the cumulated field of plasticity for the same oxide thickness of 2.75 µm has been plot for both cases #4 and #5, Figures 8(a) and (b). For accelerated oxidation kinetic, this corresponds to 2 cycles as compared to Fig. 5(c) plot for 10 cycles. It is obvious that for the realistic oxidation kinetic, the level of cumulated plasticity is much higher than for the accelerated one. This could be associated to an increase of the stress relaxation during oxide growth considering the realistic case.

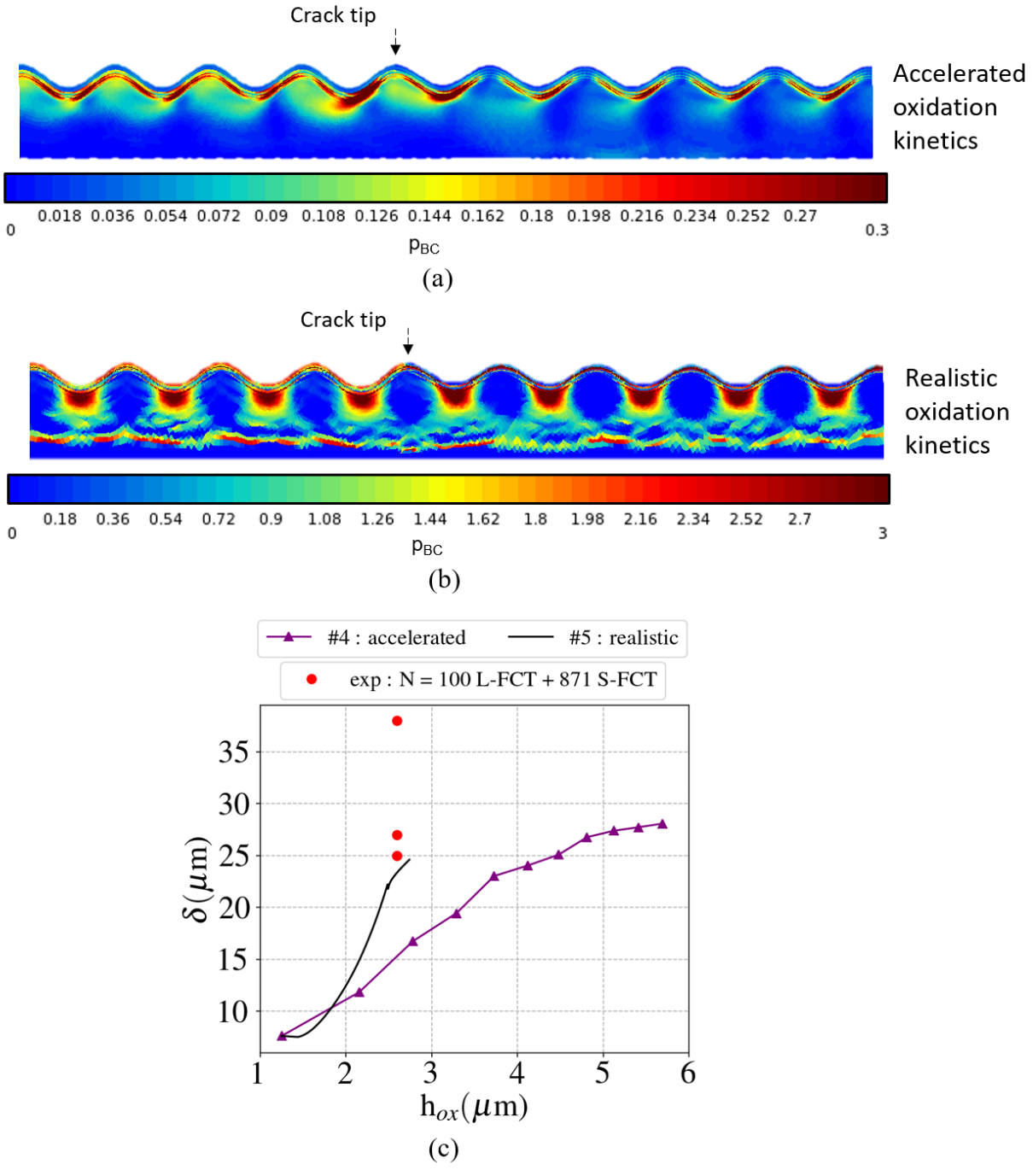

Figure 8: Cumulated plasticity in the BC layer (a) 10 cycles with accelerated oxidation kinetic (case #4) (b) 1000 cycles with realistic oxidation kinetic (case #5) and (c) comparison of blistering evolution for both cases #4 and #5

The final blister height is higher in case #5 than observed in case #4 for a given oxide thickness, Figure 8(c). When using the realistic model of oxidation, the experimental points corresponding to 100 L-FCT + 871 S-FCT as described in Figure 3, can be added to this plot. Both models reach consistent blister height as compared to experiment, but with large differences in cycle number, 10 and 1000 cycles, and TGO height, 2.8 µm and 5.8 µm for accelerated and

realistic oxidation rates respectively. This shows the capability of the method to describe experimental results, with additional tuning of the creep and oxidation kinetics. This paves the way to inverse analysis for mechanical behavior characterization from blistering measurement.

The blister height predicted by the proposed model is close to minimum blister height observed experimentally. Since all others model assumptions (cases #1 to 3) induced lower blistering, this reinforces the chosen reference model and validates the sensitivity analysis proposed in this study.

7. Conclusion

This study is based on an analysis of the evolution of a blister during thermal cycling in a TBC system. The initial blister is processed by a laser shock, thanks to the LASAT method. This is a way to monitor easily its evolution since blistering is observed in most of EB-PVD TBC systems before final TC spallation. This new laser-aided methodology developed for the characterization of TBCs properties is introduced here as LASDAM for LAser Shock for DAmage Monitoring. In the experimental part of this paper, a significant evolution of the blister height was shown with respect to the number of thermal cycles and for a fixed debonded diameter. This confirms experimentally that thermal cycling affects the mechanical state in a blister. Thanks to the sensitivity analysis achieved on a FE model, the major finding is that the growth of the blister height is due to the combination of growth strain within the oxide layer, partial stress relaxation in the plane of the interface and an increase of the strain localization in the BC layer correlated to the local interfacial roughness. The fact that the delamination is stable (no significant crack growth measured), while the blister height increases, can be the result of negative stress values at the crack tip considering local rough interface. The only way to obtain further delamination observed experimentally should be the coalescence between the large interfacial crack stopped in a crest (due to crack closure) and micro-cracking at the next valley of the rough interface. In a nutshell, the driving forces for rumpling are shown in this study to be also the driving forces for blistering, known to be a major damage mode in TBC systems, and refered to as blister driven delamination. The plastic hinge and the torque increase finally clarify the blister height increase.

As a clear perspective to this work, the temperature gradient in the TBC system and the role of local sintering of the TC layer observed in service due to surface extreme temperature associated to the flame or CMAS impact could be further analyzed.

Acknowledgements

This work was funded by Safran Tech and supported by Mark Harvey, whom we would like to thank. We would also like to acknowledge Gérard Brabant and Sylvain Gailliegue (Mines Paris, CDM) for their support during LASAT experiments and thermal cycling, respectively. Additionally, we acknowledge Dana Cosson for conducting thermal cycling at Safran Tech. The authors would like to express their gratitude to Arjen Roos (Safran Tech) for his careful review and valuable advice on the paper.

References

[1] H. E. Evans, Oxidation failure of tbc systems: An assessment of mechanisms, Surface and Coatings Technology 206 (7) (2011) 1512 – 1521. doi:10.1016/j.surfcoat.2011.05.053.
URL http://www.sciencedirect.com/science/article/pii/S0257897211005949

[2] A. G. Evans, D. Clarke, C. Levi, The influence of oxides on the performance of advanced gas turbines, Journal of the European Ceramic Society 28 (2008) 1405–1419.

[3] R. Swadźba, J. Wiedermann, M. Hetmańczyk, L. Swadźba, B. Mendala, B. Witala, Ł. Komendera, Microstructure degradation of eb-pvd tbcs on pd–pt-modified aluminide coatings under cyclic oxidation conditions, Surface and Coatings Technology 237 (2013) 16–22.

[4] P. Sallot, V. Maurel, L. Remy, F. N'Guyen, A. Longuet, Microstructure evolution of a platinum-modified nickel-aluminide coating during thermal and thermo-mechanical fatigue, Metallurgical and Materials Transactions A 46 (10) (2015) 4589–4600. doi:10.1007/s11661-015-2857-9.
URL http://dx.doi.org/10.1007/s11661-015-2857-9

[5] I. Spitsberg, D. Mumm, A. Evans, On the failure mechanisms of thermal barrier coatings with diffusion aluminide bond coatings, Materials Science and Engineering A 394 (1-2) (2005) 176 – 191. doi:DOI:10.1016/j.msea.2004.11.038.
URL http://www.sciencedirect.com/science/article/B6TXD-4F7H57S-4/2/281c10841b390c75d6f32320f828a3f9

[6] M. Ahrens, R. Vaßen, D. Stöver, S. Lampenscherf, Sintering and creep processes in plasma-sprayed thermal barrier coatings, Journal of thermal spray technology 13 (3) (2004) 432–442.

[7] D. Zhu, S. R. Choi, R. A. Miller, Development and thermal fatigue testing of ceramic thermal barrier coatings, Surface and Coatings Technology 188-189 (2004) 146 – 152. doi:DOI:10.1016/j.surfcoat.2004.08.017.
URL http://www.sciencedirect.com/science/article/B6TVV-4DBSXH7-1/2/8988a93e1e28d4b1a8f2b69dca6a57f7
[8] M. Vidal-Setif, C. Rio, D. Boivin, O. Lavigne, Microstructural characterization of the interaction between 8ypsz (eb-pvd) thermal barrier coatings and a synthetic cas, Surface and Coatings Technology 239 (2014) 41–48.
[9] R. Naraparaju, M. Hüttermann, U. Schulz, P. Mechnich, Tailoring the eb-pvd columnar microstructure to mitigate the infiltration of cmas in 7ysz thermal barrier coatings, Journal of the European Ceramic Society 37 (1) (2017) 261–270.
[10] V. Tolpygo, D. Clarke, On the rumpling mechanism in nickel-aluminide coatings. Part I : an experimental assesment., Acta Mater. 52 (2004) 5115–5127.
[11] D. Balint, S.-S. Kim, Y.-F. Liu, R. Kitazawa, Y. Kagawa, A. Evans, Anisotropic tgo rumpling in eb-pvd thermal barrier coatings under in-phase thermomechanical loading, Acta Materialia 59 (6) (2011) 2544–2555.
[12] V. Maurel, V. A. Esin, P. Sallot, F. Gaslain, S. Gailliegue, L. Rémy, Rumpling of nickel aluminide coatings: a reassessment of respective influence of thermal grown oxide and phase transformations, Materials at High Temperatures 33 (4-5) (2016) 318–324.
[13] V. Tolpygo, D. Clarke, Surface rumpling of a (ni,pt)al bond coat induced by cyclic oxidation, Acta Mater. 48 (2000) 3283–3293.
[14] V. Tolpygo, D. Clarke, K. Murphy, Oxidation-induced failure of EB-PVD thermal barrier coatings, Surf. Coat. Technol. 146-147 (2001) 124–131.
[15] N. Yanar, F. Pettit, G. Meier, Failure characteristics during cyclic oxidation of yttria stabilized zirconia thermal barrier coatings deposited via electron beam physical vapor deposition on platinum aluminide and on nicocraly bond coats with processing modifications for improved performances, Metallurgical and Materials Transactions A 37 (5) (2006) 1563–1580.
URL http://dx.doi.org/10.1007/s11661-006-0100-4
[16] A. M. Karlsson, A. Evans, A numerical model for the cyclic instability of thermally grown oxides in thermal barrier systems, Acta Materialia 49 (10) (2001) 1793–1804.
[17] L. Berthe, M. Arrigoni, M. Boustie, J. P. Cuq-Lelandais, C. Broussillou, G. Fabre, M. Jeandin, V. Guipont, M. Nivard, State-of-the-art laser adhesion test (LASAT), Nondestructive Testing and Evaluation 26 (3-4, SI) (2011) 303–317.
[18] V. Guipont, M. Jeandin, S. Bansard, K. A. Khor, M. Nivard, L. Berthe, J.-P. Cuq-Lelandais, M. Boustie, Bond strength determination of hydroxyapatite coatings on ti-6al-4v substrates using the laser shock adhesion test (lasat), Journal of Biomedical Materials Research Part A 95 (4) (2010) 1096–1104.
[19] V. Guipont, G. Begue, G. Fabre, V. Maurel, Buckling and interface strength analyses of eb-pvd tbc combining laser shock adhesion test (lasat) to thermal cycling, Surf. Coat. Technol. under edition (special issue 46th ICMCTF). doi:https://doi.org/10.1016/j.surfcoat.2019.124938.
URL http://www.sciencedirect.com/science/article/pii/S0257897219309193
[20] V. Maurel, V. Guipont, M. Theveneau, B. Marchand, F. Coudon, Thermal cycling damage monitoring of thermal barrier coating assisted with lasat (laser shock adhesion test), Surface and Coatings Technology 380 (2019) 125048.
[21] H. Sapardanis, V. Maurel, A. Köster, S. Duvinage, F. Borit, V. Guipont, Influence of macroscopic shear loading on the growth of an interfacial crack initiated from a ceramic blister processed by laser shock, Surface and Coatings Technology 291 (2016) 430–443.
[22] V. Maurel, L. Mahfouz, V. Guipont, B. Marchand, F. Gaslain, A. Koster, A. Dennstedt, M. Bartsch, F. Coudon, Recent progress in local characterization of damage evolution in thermal barrier coating under thermal cycling, Superalloys 2020 (2020) 813–823.
[23] V. Maurel, M. Bartsch, M.-H. Vidal-Sétif, R. Vaßen, V. Guipont, Coated single crystal superalloys: processing, characterization, and modeling of protective coatings, in: Nickel Base Single Crystals Across Length Scales, Elsevier, 2022, pp. 283–338.
[24] J. Hutchinson, M. Thouless, E. Liniger, Growth and configurational stability of circular, buckling-driven film delaminations, Acta Metallurgica et Materialia 40 (2) (1992) 295 – 308. doi:DOI:10.1016/0956-7151(92)90304-W.
URL http://www.sciencedirect.com/science/article/B7599-48CXHGY-PT/2/87022e2d285c516d0f143d9fcb220e20
[25] P. Y. Thery, M. Poulain, M. Dupeux, M. Braccini, Spallation of two thermal barrier coating systems: experimental study of adhesion and energetic approach to lifetime during cyclic oxidation, Journal of Materials Science 44 (7) (2009) 1726–1733. doi:{10.1007/s10853-008-3108-x}.
[26] J.-R. Vaunois, M. Poulain, P. KanoutÃ©, J.-L. Chaboche, Development of bending tests for near shear mode interfacial toughness measurement of eb-pvd thermal barrier coatings, Engineering Fracture Mechanics 171 (2017) 110 – 134. doi:https://doi.org/10.1016/j.engfracmech.2016.11.009.
URL http://www.sciencedirect.com/science/article/pii/S0013794416305860
[27] T. Perez, D. Monceau, C. Desgranges, Kinetic oxidation model including the transient regime for a single crystal nickel-based superalloy over the temperature range 750–1300° c, Corrosion Science 206 (2022) 110485.
[28] C. Courcier, V. Maurel, L. Remy, S. Quilici, I. Rouzou, A. Phelippeau, Interfacial damage based life model for eb-pvd thermal barrier coating, Surface and Coatings Technology 205 (13-14) (2011) 3763 – 3773. doi:DOI:10.1016/j.surfcoat.2011.01.008.
URL http://www.sciencedirect.com/science/article/B6TVV-51Y57FC-4/2/d26ec16a1de5b850aa59dce80eaa469c
[29] B. R. Akula, J. Vignollet, V. A. Yastrebov, Mortex method for contact along real and embedded surfaces: coupling x-fem with the mortar method, arXiv preprint arXiv:1902.04000.
[30] J. Frachon, Multiscale approach to predict the lifetime of eb-pvd thermal barrier coatings, Ph.D. thesis, Mines ParisTech (14 Decembre 2009).
[31] E. Busso, H. Evans, Z. Qian, M. Taylor, Effects of breakaway oxidation on local stresses in thermal barrier coatings, Acta Materialia 58 (4) (2010) 1242 – 1251. doi:DOI:10.1016/j.actamat.2009.10.028.
URL http://www.sciencedirect.com/science/article/B6TW8-4XP8B5F-4/2/87bf9bc3a37b39e8fa685984b090f994
[32] T. Hille, S. Turteltaub, A. Suiker, Oxide growth and damage evolution in thermal barrier coatings, Engineering Fracture Mechanics 78 (10) (2011) 2139 – 2152. doi:10.1016/j.engfracmech.2011.04.003.
URL http://www.sciencedirect.com/science/article/pii/S0013794411001421
[33] A. Freborg, B. Ferguson, W. Brindley, G. Petrus, Modeling oxidation induced stresses in thermal barrier coatings, Materials Science and Engineering: A 245 (2) (1998) 182–190.

[34] K. Sfar, J. Aktaa, D. Munz, Numerical investigation of residual stress fields and crack behavior in tbc systems, Materials Science and Engineering: A 333 (1-2) (2002) 351–360.
[35] Z.-Y. Wei, H.-N. Cai, S.-D. Zhao, G.-R. Li, W.-W. Zhang, A. Tahir, Dynamic multi-crack evolution and coupling tbc failure together induced by continuous tgo growth and ceramic sintering, Ceramics International 48 (11) (2022) 15913–15924.
[36] E. Busso, Z. Qian, M. Taylor, H. Evans, The influence of bondcoat and topcoat mechanical properties on stress development in thermal barrier coating systems, Acta Materialia 57 (8) (2009) 2349 – 2361. doi:DOI:10.1016/j.actamat.2009.01.017.
URL http://www.sciencedirect.com/science/article/B6TW8-4VV0DMW-2/2/a78caf87a8bbcbfe80441433bf33910f
[37] D. Texier, D. Monceau, S. Selezneff, A. Longuet, E. Andrieu, High temperature micromechanical behavior of a pt-modified nickel aluminide bond-coating and of its interdiffusion zone with the superalloy substrate, Metallurgical and Materials Transactions A (2020) 1–6.
[38] A. Karlsson, J. Hutchinson, A. Evans, The displacement of the thermally grown oxide in thermal barrier systems upon temperature cycling, Mater. Sci. Engng. A351 (2003) 244–257.
[39] J. Lemaitre, J. L. Chaboche, Mechanics of Solid Materials, Cambridge University Press, 1990.
[40] D. Pan, M. Chen, P. Wright, K. Hemker, Evolution of a diffusion aluminide bond coat for thermal barrier coatings during thermal cycling, Acta Materialia 51 (8) (2003) 2205 – 2217. doi:10.1016/S1359-6454(03)00014-4.
URL http://www.sciencedirect.com/science/article/pii/S1359645403000144
[41] M. Z. Alam, S. Kamat, V. Jayaram, D. K. Das, Tensile behavior of a free-standing pt-aluminide (ptal) bond coat, Acta materialia 61 (4) (2013) 1093–1105.
[42] Safran, internal report, Tech. rep., Safran.
[43] E. Busso, J. Lin, S. Sakurai, A mechanistic study of oxydation-induced degradation in a plasma-sprayed thermal barrier coating system. Part I: model formulation, Acta Mater. 49 (2001) 1515–1528.
[44] T. Hille, A. Suiker, S. Turteltaub, Microcrack nucleation in thermal barrier coating systems, Engineering Fracture Mechanics 76 (6) (2009) 813 – 825. doi:10.1016/j.engfracmech.2008.12.010.
URL http://www.sciencedirect.com/science/article/pii/S0013794408003330